A Multi-Resonant Converter for Non-Contact Charging with Electromagnetic Coupling

R. Laouamer, M. Brunello, J.P. Ferrieux
Laboratoire d'Electrotechnique de Grenoble
INPG / UJF.UMR.CNRS 5529
ENSIEG, BP. 46, 38402 Saint Martin d'Hères Cedex France
Tel: (33) 4 76 82 62 99, Fax: (33) 4 76 82 63 00
E-mail: Rachid.Laouamer @ leg.ensieg.inpg.fr

O. Normand, N. Buchheit
EDF (**E**lectricité **D**e **F**rance),
Research and **D**evelopment **D**ivision (DER)
1, Avenue G. de Gaulle - 92141 Clamart Cedex France
Tel: (33) 1 47 65 31 63, Fax: (33) 1 47 65 39 11
E-mail: Nicolas.Buchheit @ der.edfgdf.fr

Abstract - Parallel resonant converter type (PRC-LLCC) is analyzed in a case of an automatic inductive charging application. The tank circuit of this converter consists of leakage inductance, magnetizing inductance and two capacitors with an inductive output filter. This converter allows the transfer of power without oversizing the inverter and a soft-switching mode of the transistors. The soft-switching mode and the sensitivity to the load variation, the coupling factor and the air gap (6-8 mm) are studied using the first harmonic method. The choice of the working range and the validity limit of the analyze method are presented. Theoretical results are validated experimentally with a 3 kW prototype.

I. INTRODUCTION

Inductive charging is a method for magnetic-transfer of power which offers several advantages for fully automatic electrical vehicle (EV) charging stations, such as the possibility to avoid a complex and expensive active alignment system between the car and the electrical power station.

In our application the cars will be parked in pre-defined parking positions where the automatic chargers are fitted (Fig. 1). The charging process is fully automatic without any driver intervention.

As shown in Fig.1 the coupler is located under the EV. The mechanical protection of the transformer part which is integrated into EV is achieved by an isolating layer. This layer results in a large air gap between the secondary and the primary winding of the transformer (6 mm ~ 8 mm).

In order to reach the high frequencies (20 to 50 kHz) and to transfer the high power (3 to 36 kW) needed by this application, a resonant converter is the most common solution. Interest in resonant converters has recently shifted to higher-order topologies in which circuit parasitic components are taken into account or additional elements are added to achieve improved operating characteristics. Two element and three element resonant circuits, LCC-type and LLC-type [1,3,4,5] have been comprehensively discussed and analyzed. Four element and higher order topologies provide many variations with unique characteristics. But these have not been comprehensively treated in the literature due to their complexity and number [6]. In this study, higher order topology models are considered in order to include in the analysis the effect of the leakage and magnetizing inductances of the coupler.

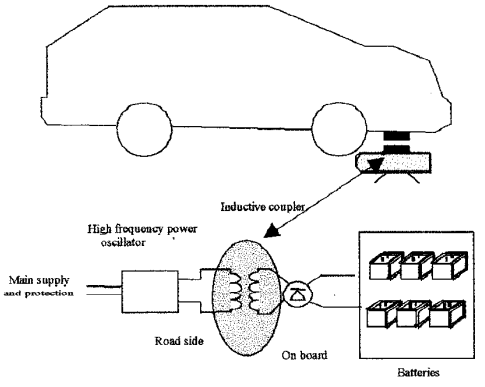


Fig. 1. Basics components of the charging system

II. THE INDUCTIVE COUPLER

The coupler is based on the pot core design shown in Fig. 2, taken from Siemens.

Fig. 3 shows the open circuit frequency characteristics of the transformer which is measured by an impedance analyzer (HP 4194A).

To minimize the skin effect, Litz conductors are used for the windings. The effect of the parasitic capacitors appears at frequencies higher than 1 MHz (Fig. 3). As the converter works at frequencies lower than 100 kHz, the equivalent circuit derived by [2] can be simplified. The final equivalent asymmetric circuit is composed of the magnetic inductance (L_p) and the leakage inductance (L_s), Fig. 4.

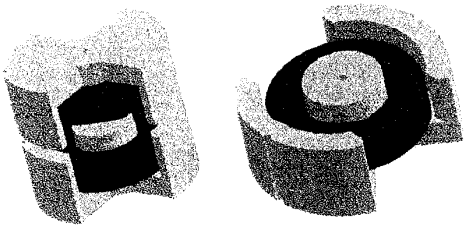


Fig. 2. Geometry of the pot core

0-7803-3932-0

Authorized licensed use limited to: University of Maryland College Park. Downloaded on May 14,2026 at 20:17:40 UTC from IEEE Xplore. Restrictions apply.

IPR2026-00379
Tesla EX1016 Page 1

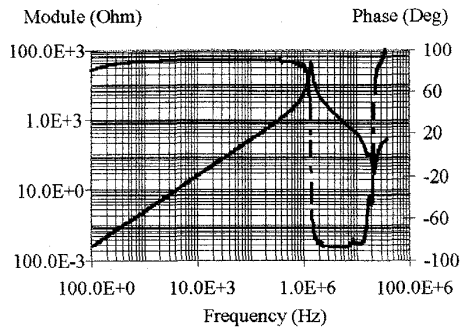


Fig. 3. Characterisation results

We have :

$L_s = L_{10} \cdot (1-k^2)$ and $L_p = L_{10} \cdot k^2$, where :

L_{10} : Primary open circuit inductance.

k : Coupling factor

m : Transformation ratio

III. THE RESONANT CONVERTER

The circuit diagram of this topology is shown in Fig. 5. The two main reasons for selecting this circuit topology are: this four order converter operates without the resonant converter usual oversizing of the inverter switches and only small variations of its switching frequency are required in a large operating range, which facilitates the EMC filtering.

A. Analysis

The four element LLCC converter has previously been analyzed with an inductive output filter [5] and a capacitive filter [6]. The analysis of such a converter is complex because the parallel inductance (magnetizing inductance), the series inductance (leakage inductance) and the coupling factor are interdependent. Therefore we propose to analyze the circuit by using fundamental mode analysis (FMA).

The FMA, also called the first harmonic method, provides a simplified approach to analyze this converter. It is based on the calculation of the first harmonic components of the circuit variables. The fundamental component of the inverter output voltage is computed using the Fourier's series. The fundamental mode equivalent circuit is shown in Fig. 6, with the following parameter values :

$$C_p = \frac{m^2}{k^2}.C_r \,,\; R = \frac{\pi^2.k^2}{8.m^2}.R_s,\; e_{max} = \frac{4.E}{\pi} \qquad (1)$$

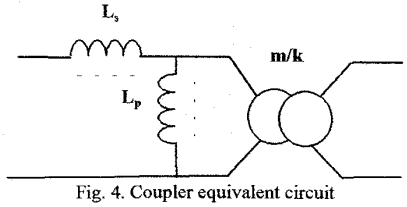


Fig. 4. Coupler equivalent circuit

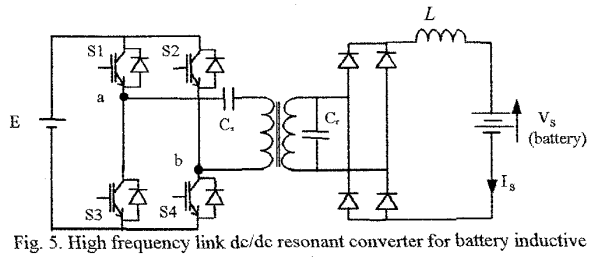


Fig. 5. High frequency link dc/dc resonant converter for battery inductive charging

R_s is the equivalent load resistance and is defined as the ratio between the battery voltage V_s and the battery current I_s (V_s=R_s.I_s).

Using ordinary circuit analysis the input impedance Z_i can be computed (as shown in Appendix A) and has the following simplified form:

$$Z_i = \frac{R \cdot (1-(1+K_W^2+K_L)\cdot\Omega^2+K_W^2\cdot\Omega^4)}{-K_L\cdot\Omega^2+\frac{j\cdot R}{Z_S}\cdot(\Omega-K_W^2\cdot\Omega^3)} + \frac{j\cdot Z_S\cdot K_L\cdot(\Omega-\Omega^3)}{-K_L\cdot\Omega^2+\frac{j\cdot R}{Z_S}\cdot(\Omega-K_W^2\cdot\Omega^3)} \qquad (2)$$

Ω : Normalized frequency with the base frequency f_b.

$$f_b = f_S = \frac{1}{2.\pi.\sqrt{L_S.C_S}} \qquad (3)$$

$$f_p = \frac{1}{2.\pi.\sqrt{L_p.C_p}},\; Z_S = \sqrt{\frac{L_S}{C_S}} \qquad (4)$$

$$K_L = \frac{k^2}{1-k^2},\; K_W = \frac{f_S}{f_p} \qquad (5)$$

The phase shift of the input impedance Z_i defines the switching mode of the switches. A positive phase shift causes a Zero Voltage Switching (ZVS) mode and a negative phase shift a Zero Current Switching (ZCS) mode. The load variation (charging state of battery), the coupling factor and the air gap have an important influence on the switching mode.

B. Sensitivity to the load variation (charging state of battery)

Fig. 7. presents the phase shift of the input impedance Z_i according to the equivalent load resistance R_s and the normalized frequency Ω. The other computation parameters

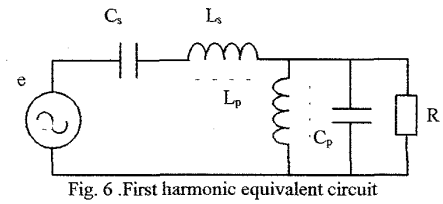


Fig. 6 .First harmonic equivalent circuit

Authorized licensed use limited to: University of Maryland College Park. Downloaded on May 14,2026 at 20:17:40 UTC from IEEE Xplore. Restrictions apply.

IPR2026-00379
Tesla EX1016 Page 2

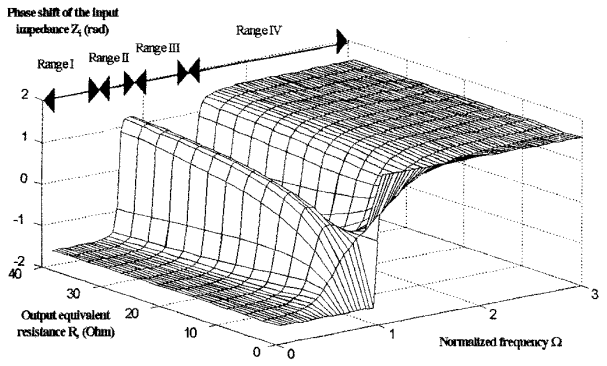


Fig. 7. Influence of the load on the switching mode

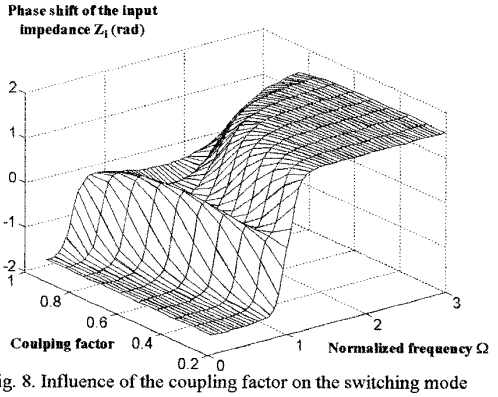


Fig. 8. Influence of the coupling factor on the switching mode

are : L_S=258µH, C_S =150nF, m=0.26, k =0.6 and K_W=1.

Depending on the load, there can be either two or four frequency ranges with different switching modes.

C. Sensitivity to the coupling factor

Another important parameter is the coupling factor. The evaluation of the input impedance phase shift as function of this factor is shown in Fig. 8 using (2), L_S=258µH, C_S =150nF, R_s=8, m=0.26 and K_W=1. The validity of the results is discussed in chapter VI.

D. Output characteristics.

x and y are, respectively, the normalized converter output current and the normalized converter output voltage with the base quantities $I_b = \frac{E}{Z_S}.\frac{k}{m}$ and $V_b = E.\frac{m}{k}$.

Fig. 9 represents the output characteristics for the four presented frequency ranges of fig 7, distinguished by their switching mode. For our application, we have $R_s \geq 8\Omega$, which corresponds to a 3 kW maximum output power.

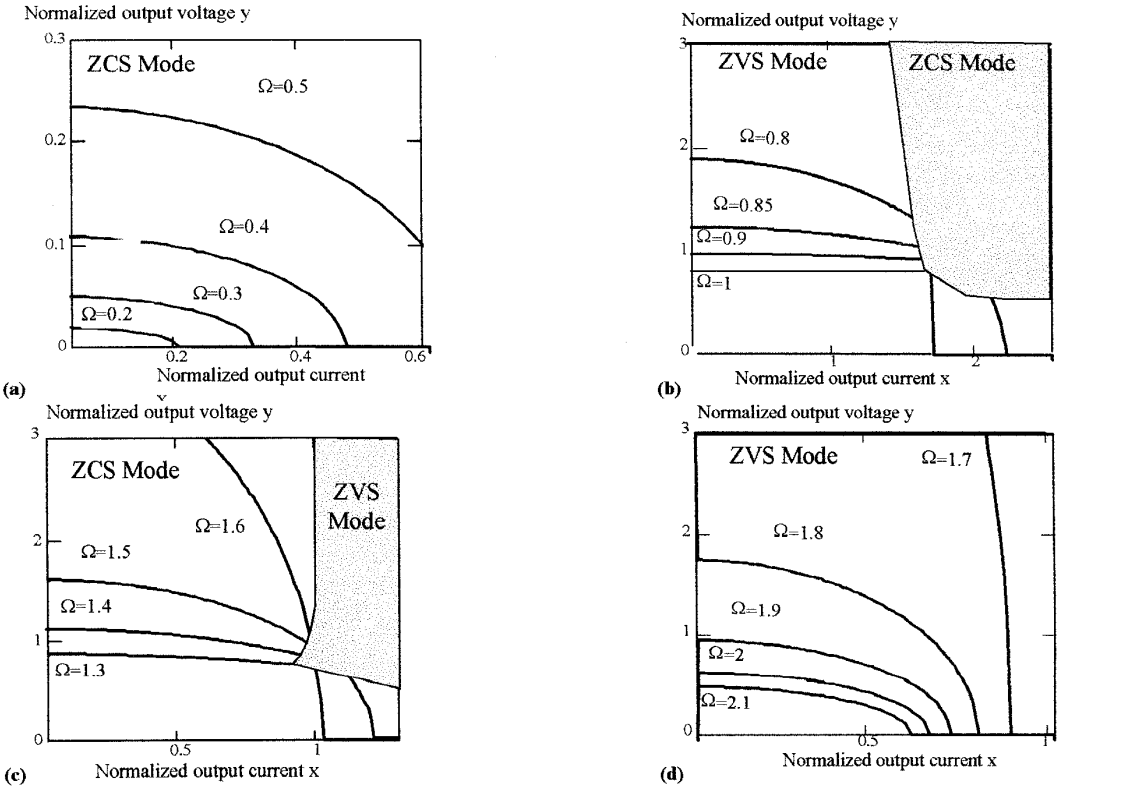


Fig. 9. Converter output characteristics according to the normalized frequency Ω : **a)** Range I, **b)** Range II, **c)** Range III, **d)** Range IV

Authorized licensed use limited to: University of Maryland College Park. Downloaded on May 14,2026 at 20:17:40 UTC from IEEE Xplore. Restrictions apply.

IPR2026-00379
Tesla EX1016 Page 3

We have the following equation, using (11) from appendix B:

$$y = \frac{8}{\pi^2} \cdot \sqrt{\frac{1-\left(\frac{\Omega^2-1}{\Omega}\right)^2 \cdot x^2}{\left(1+\frac{1}{K_L}\cdot\left(1+K_W^2-K_W^2\cdot\Omega^2-\frac{1}{\Omega^2}\right)\right)^2}} \quad (6)$$

E. Choice of the working range

Comparing with ZCS, several advantages of ZVS can be observed:

- IGBT's turn on is effected at zero voltage and zero current which reduces the turn-on losses.
- the parasitic capacitor between drain and source improves the commutation. A supplementary further capacitor can be connected between drain and source for the decrease of these losses.
- there is no need for fast recovery anti parallel diodes.

In order to have the ZVS advantages, the ranges II and IV should be chosen. Low variation of the frequency results in a higher variation of the normalized output current in range II compared to that of range IV. Fig. 10 represents the inverter output peak currents of range II. These traces are represented at different levels of normalized output voltage. It is shown that the circulation current decreases with the load; this accounts for the high efficiency at light-load.

IV. EXPERIMENTAL RESULTS

Based on the theoretical analysis, a 3 kW prototype resonant converter is designed. Experimental results are shown in Table 1.

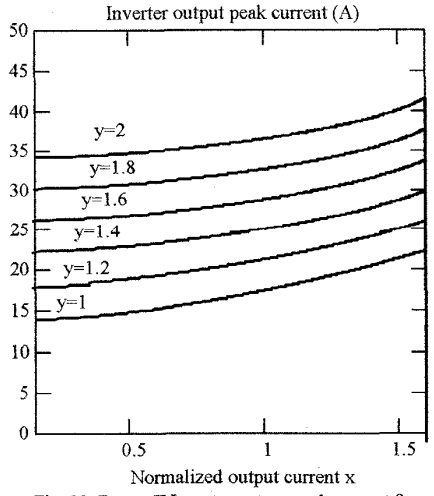


Fig. 10. Range II Inverter output peak current for different normalized output voltage y.

Table 1. Experimental results

Parameters	Values
Inverter output peak voltage (V)	344
Inverter output rms. current (A)	10
Inverter output peak current (A)	13.2
Transformer secondary rms. current (A)	31.5
Transformer secondary peak current (A)	45
Transformer secondary rms. voltage (V)	182
Transformer secondary peak voltage (V)	288
Input voltage (DC) (V)	325
Input current (A)	10
Output voltage (V)	156
Output current (A)	19.3
Output power (kW)	3
efficiency (%)	89

A. Sensitivity to the air gap

As already mentioned this charger operates with a large air gap (6 mm ~ 8 mm). Air gap variations cause a variation on the coefficient K_w (series resonant frequency to parallel resonant frequency ratio). K_w value influences converter operating characteristics, as shown in Fig. 11 with the theoretical phase shift of the input impedance Z_i as example.

In Fig. 12, experimental output characteristics are plotted and confirm the sensitivity to air gap. These traces are represented for different air gaps. At fixed frequencies, the output voltage increases with the increase of the air gap. This phenomenon is due to the resonant network. The

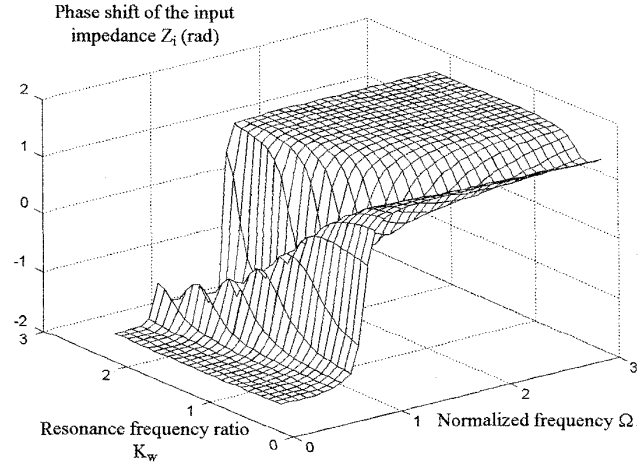


Fig. 11. Influence of K_w on the switching mode

Authorized licensed use limited to: University of Maryland College Park. Downloaded on May 14,2026 at 20:17:40 UTC from IEEE Xplore. Restrictions apply.

IPR2026-00379
Tesla EX1016 Page 4

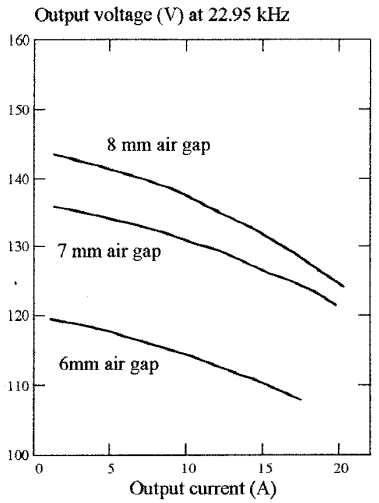


Fig. 12. Experimental output characteristics with different air gaps

decrease of the coupling factor k involves the increase of $\frac{m}{k}$ ratio and the series-resonant frequency is close to the switching frequency. It is however possible to control the output current value independently of the air gap by adjusting the inverter frequency, as demonstrated by the prototype.

V. THE COMPARISON OF THE THEORETICAL AND THE EXPERIMENTAL RESULTS

The component values of the prototype were derived

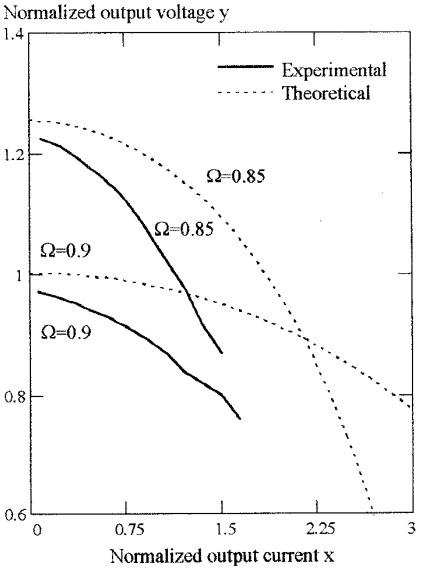


Fig. 13. Theoretical and experimental output characteristics

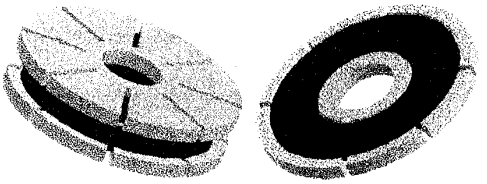


Fig. 14. Inductive coupler with a higher coupling factor

using the first harmonic method. The experimental results, especially for full load case, confirm this proceeding. Fig. 13 compares at different frequencies the theoretical and the experimental results. In practice, the differences between the theoretical and the experimental curves are due to some circuit losses which are not taken into consideration in the theoretical analysis and the assumptions of the FMA.

VI. THE VALIDITY LIMIT OF THE FIRST HARMONIC METHOD

It is important to be sure that the assumptions of the FMA are valid. The resonant circuit voltages and currents shapes have to be nearly sinusoidal. In particular, the further the frequency is from the resonant frequencies of the circuit, the more the FMA analysis is approximate. In the case of the coupler of Fig. 2 with a low coupling factor, the agreement between the theoretical and the experimental results is sufficient.

The first harmonic method is then tested using another inductive coupler [7], Fig. 14. The coupler is much larger and has a lower profile than the first one. It has therefore higher coupling factor (~ 0.9). However, in the operating range ($0.7<\Omega<1$), its ratio between the input impedance Z_i for first and for the third harmonic is higher than 2, whereas the same ratio for the first coupler (Fig. 2.) is lower than 0.25. Fig. 15 shows an example at normalized frequency $\Omega=0.77$. It means than the resonant circuit will be excited by the third harmonic voltage components of the inverter and

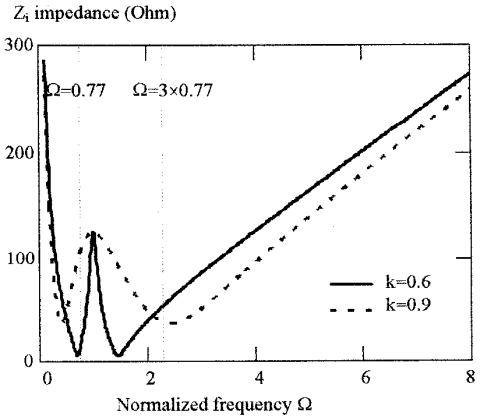


Fig. 15. Module of Zi with different coupling factor

Authorized licensed use limited to: University of Maryland College Park. Downloaded on May 14,2026 at 20:17:40 UTC from IEEE Xplore. Restrictions apply.

IPR2026-00379
Tesla EX1016 Page 5

that the voltages and currents shapes of the resonant circuit will be distorted by the third harmonic components. As a result, the fundamental mode analysis is not valid for high coupling factors.

VII. CONCLUSION

In this paper, the multi-element, multi-resonant topology is analyzed using the first harmonic method. The equations were generated and solved. As a conclusion, the circuit is built and an excellent agreement is found between analytical and experimental data. However, the first harmonic method can be applied only to a high inductive coupler with a low coupling factor.

REFERENCES

[1] J.-P. Ferrieux, F. Forest, "Alimentation à découpage convertisseur à résonance:principes-composants-modélisation" Editions Masson, 1994.

[2] B. Cogitore,J.-P. Keradec, J. Barbaroux, "The two-winding transformer: An experimental method to obtain a wide frequency range equivalent circuit" IEEE, Transactions on Instr. And Measu., april 1994.

[3] A. Esser, " Contactless Charging and Communication for Electric Vehicles " IEEE, Industry Applications Magazine, November/ December 1995.

[4] K.W. Klontz, D.M. Divan, D.W. Novotny, R.D. Lorenz, " Converter selectionfor Electric Vehicle Charger Systems with a high-power link " IEEE, Industry Application Society, 1993, pp. 855-861.

[5] HLN. Weigemann, D.W. Novotny, D.M. Divan, R. Mohan, " A ZVS.Dual Resonant Converter for Battery Charging Applications " Power Electronics Specialists Conference, 1991.

[6] J. Hayes, J. Hall, M. Egan, J.M.D. Murphy, " Full-bridge, series resonant converter supplying the SAE J-1773 Electric Vehicle Inductive Charging Interface " IEEE, pp.1913-1918, 1996.

[7] C.A. Bleijs, O. Normand, " A fully automatic station using inductive charging techniques" Paper No. 4G.02, presented at the EVS-13, Osaka-Japan (September 1996).

APPENDIX A

Using ordinary circuit analysis for the circuit in Fig. 7 following equations can be computed

$$Z_1 = \frac{R.j\omega.L_p}{R - R\omega^2.L_p.C_p + j\omega.L_p} \qquad (7)$$

and

$$Z_2 = \frac{1}{j\omega.C_s} + j\omega.L_s = \frac{1-\omega^2.L_s.C_s}{j\omega.C_s} \qquad (8)$$

also

$$Z_i = Z_1 + Z_2$$

then

$$Z_i = \frac{A+B}{C}$$

where

$$A = R\omega^4.L_s.L_p..C_s.C_p + j.(\omega.L_p - \omega^3.L_s.L_p.C_s)$$

$$B = R - R\omega^2.L_p.C_p - R\omega^2.L_s.C_s - R\omega^2.L_p.C_s$$

$$C = -\omega^2.L_p.C_s + j.(R\omega.C_s - R\omega^3.L_p.C_p.C_s)$$

APPENDIX B

Using DC value of voltage across C_p output voltage can be computed

$$V_S = \frac{2}{\pi}.\left(\frac{m}{K}.V_{Cp\max}\right) \qquad (9)$$

then

$$V_S = \frac{2}{\pi}.\frac{m}{K}\frac{4.E}{\pi}.\frac{Z_1}{Z_1+Z_2} \qquad (10)$$

and finally

$$V_S = \frac{2.m}{\pi.k}.\frac{4.E}{\pi}.\frac{D}{E+j.H} \qquad (11)$$

$$D = -R\omega^2.L_p.C_s$$

$$E = R.(1-\omega^2.(L_p.C_s - L_p.C_p - L_s.C_s) + \omega^4.L_s.C_s.L_p.C_p)$$

$$H = \omega.L_p - \omega^3.L_p.L_s.C_s$$

Authorized licensed use limited to: University of Maryland College Park. Downloaded on May 14,2026 at 20:17:40 UTC from IEEE Xplore. Restrictions apply.

IPR2026-00379
Tesla EX1016 Page 6